

DISCOVERY AND VALIDATION OF A HIGH-DENSITY SUB-NEPTUNE FROM THE K2 MISSION

NÉSTOR ESPINOZA^{1,2}, RAFAEL BRAHM^{1,2}, ANDRÉS JORDÁN^{1,2}, JAMES S. JENKINS³, FELIPE ROJAS¹, PAULA JOFRÉ⁴, THOMAS MÄDLER⁴, MARKUS RABUS^{1,5}, JULIO CHANAMÉ^{1,2}, BLAKE PANTOJA³, MARITZA G. SOTO³, KATIE M. MORZINSKI⁶, JARED R. MALES⁶, KIMBERLY WARD-DUONG⁷, LAIRD M. CLOSE⁶

Draft version June 29, 2021

ABSTRACT

We report the discovery of BD+20594b, a high density sub-Neptune exoplanet, made using photometry from Campaign 4 of the two-wheeled Kepler (K2) mission, ground-based radial velocity follow-up from HARPS and high resolution lucky and adaptive optics imaging obtained using AstraLux and MagAO, respectively. The host star is a bright ($V = 11.04$, $K_s = 9.37$), slightly metal poor ($[\text{Fe}/\text{H}] = -0.15 \pm 0.05$ dex) solar analogue located at $152.1_{-7.4}^{+9.7}$ pc from Earth, for which we find a radius of $R_* = 0.928_{-0.040}^{+0.055} R_\odot$ and a mass of $M_* = 0.961_{-0.029}^{+0.032} M_\odot$. A joint analysis of the K2 photometry and HARPS radial velocities reveal that the planet is in a ≈ 42 day orbit around its host star, has a radius of $2.23_{-0.11}^{+0.14} R_\oplus$, and a mass of $16.3_{-6.1}^{+6.0} M_\oplus$. Although the data at hand puts the planet in the region of the mass-radius diagram where we could expect planets with a pure rock (i.e. magnesium silicate) composition using two-layer models (i.e., between rock/iron and rock/ice compositions), we discuss more realistic three-layer composition models which can explain the high density of the discovered exoplanet. The fact that the planet lies in the boundary between “possibly rocky” and “non-rocky” exoplanets, makes it an interesting planet for future RV follow-up.

Keywords: kepler, exoplanets

1. INTRODUCTION

Since the discovery of the first rocky exoplanet (term we use here to refer to planets with masses and radii consistent with MgSiO_3 and Fe compositions following Rogers, 2015), CoRoT-7b (Léger et al., 2009; Queloz et al., 2009), effort has been made to find and study the formation, composition and evolution of these systems, since they resemble Earth in many ways. As most rocky planets are smaller in size than $1.6R_\oplus$, which correspond to masses of $6M_\oplus$ (Weiss & Marcy, 2014; Wolfgang & Lopez, 2015; Rogers, 2015), the discovery of those type of exoplanets is difficult due to the small signals that these radii and masses imply. In fact, in addition to CoRoT-7b, only 9 planets with secure masses and radii (i.e., masses and radii with values more than $3 - \sigma$ away from zero) in this rocky regime exist to date: GJ1132 (Berta-Thompson et al., 2015), Kepler-36b (Carter et al., 2012), K2-3d (Crossfield et al., 2015; Almenara et al., 2015), Kepler-93b (Dressing et al., 2015), Kepler-10b (Dumusque et al., 2015; Weiss et al., 2016), Kepler-23b (Ford et al., 2012; Hadden & Lithwick, 2014), Kepler-20b (Fressin et al., 2012), Kepler-406b (Marcy et al., 2014), and Kepler-78b (Sanchis-Ojeda et al., 2013;

Howard et al., 2013; Pepe et al., 2013; Grunblatt et al., 2015). All of these planets have radii smaller than $\sim 1.6R_\oplus$, as has been empirically determined.

Although the sample of rocky planets is small, some interesting relationships suggest that some of these rocky planets might have common properties (Weiss & Marcy, 2014). Perhaps one of the most interesting relations was recently introduced by Dressing et al. (2015) which, considering the planets with radii and mass measurements measured to better than 20% precision, show that the planets follow a common iso-composition curve on the mass-radius diagram, along with Earth and Venus. This relation was recently revised by Zeng, Sasselov & Jacobsen (2016) to be a 74% rock and 26% Fe composition. This suggests that these small, rocky analogs of Earth might have similar compositions with small intrinsic scatter.

Here we report what could be a possible interesting addition to the picture of rocky worlds described above: a $2.23R_\oplus$ exoplanet that falls just where a pure rock (i.e., magnesium silicate) composition is expected in the mass radius diagram using two-layer models. Although this does not mean the planet has exactly this composition, its position on the diagram does makes it interesting due the fact that this has been used in previous works to divide the “non-rocky” and “possibly rocky” planets (Rogers, 2015). The discovery is made in the context of a Chilean based effort whose aim is to follow-up planetary candidates selected using data from the two-wheeled *Kepler* (K2) mission. K2 has proven to be very effective in the search for exoplanets, enabling a plethora of new discoveries of planets of different sizes, which are especially interesting due to the presence of several bright host stars in the sample that allow detailed follow-up characterisation (see, e.g., Armstrong et al., 2015; Becker et al., 2015; Crossfield et al., 2015; Petigura et al., 2015;

¹ Instituto de Astrofísica, Facultad de Física, Pontificia Universidad Católica de Chile, Av. Vicuña Mackenna 4860, 782-0436 Macul, Santiago, Chile

² Millennium Institute of Astrophysics, Av. Vicuña Mackenna 4860, 782-0436 Macul, Santiago, Chile

³ Departamento de Astronomía, Universidad de Chile, Camino al Observatorio, Cerro Calán, Santiago, Chile

⁴ Institute of Astronomy, University of Cambridge

⁵ Max Planck Institute for Astronomy, Heidelberg, Germany

⁶ Steward Observatory, University of Arizona, 933 N. Cherry Ave, Tucson, AZ 85721-0065 USA

⁷ School of Earth and Space Exploration, Arizona State University, Tempe, AZ, 85287, USA

Sanchis-Ojeda et al., 2015; Vanderburg et al., 2015).

The paper is structured as follows. In §2 we present the data, which includes the K2 photometry, archival, new, adaptive optics (AO) and lucky imaging of the target star, along with high resolution spectra and radial velocities obtained with the HARPS spectrograph. §3 presents a joint analysis of the data and presents the derived parameters of the planetary system. We discuss the results in §4 and present our conclusions in §5.

2. DATA

2.1. K2 Photometry

K2 photometry for our target was obtained by the *Kepler* spacecraft during Campaign 4. This field was observed between February and April 2015 and the data was released on September of the same year. We obtained the decorrelated versions of all the lightcurves in the campaign which were made publicly available for download by Vanderburg & Johnson (2014), using the photometry with the optimal aperture, which in the case of our target star corresponded to a ≈ 3 pixel radius around the target, or an aperture of $\approx 12''$ radius. We performed a transit search using a Box Least Squares (BLS, Kovács, Zucker & Mazeh, 2002) algorithm. Once a periodic signal is detected along with the best-fit depth, the transit event is flagged as a potential planetary candidate if (1) the depth is at least 3σ larger than the average noise level of the lightcurve (denoted by σ) and (2) if there are three or more transit events. Initially, because of the last requirement, the lightcurve of the target star was not flagged by our transit search pipeline. However, we also performed visual inspection of all the lightcurves, revealing this interesting candidate. In order to double check that this was indeed an astrophysical signal and not a spurious signal arising from the decorrelation method used to obtain the lightcurve, we also inspected the detrended lightcurves released by the *Kepler* team using the PDC-MAP algorithm (Stumpe et al., 2012), and the same signal was observed at the exact same times as the signals observed in the Vanderburg & Johnson (2014) photometry. We were thus confident that the signal is of astrophysical origin and proceeded to analyse the light curve.

A median filter with a 41 point (~ 20.5 hour) window was used in order to further filter long-term variations of this target. The resulting median filter was smoothed using a Gaussian filter with a 5-point standard-deviation, and this smoothed light curve was used to normalize the light curve. Using this normalized lightcurve, an initial fit using our transit-fitting pipeline (see below) revealed a $P = 41.7d$ period for this candidate and a lightcurve whose shape resembled that of a planetary transit, with a transit duration consistent with that of a planetary companion. Using the parameters obtained from this initial fit, we removed outliers from the out-of-transit data, discarding any points deviating more than $3\text{-}\sigma$ from the median flux. The resulting normalized version of this lightcurve is shown on Figure 1. No other significant signals were found in the photometry.

2.2. Reconnaissance spectroscopy

A high resolution spectrum of this target was taken on October 21st with the CORALIE spectrograph mounted

on the 1.2m Euler Telescope in La Silla Observatory in order to obtain rough spectral parameters of the stellar host, and define whether this was a giant or a dwarf star. Data were reduced and analyzed using the procedures described in Jordán et al. (2014). The analysis of the CORALIE spectra gave $T_{\text{eff}} = 5600$ K, $\log(g) = 4.4$ dex, $[\text{Fe}/\text{H}] = 0.0$ dex and $v \sin(i) = 2.5$ km/s, which revealed that the star was a dwarf solar-type star. In addition, no secondary peak was seen on the cross-correlation function indicating no detectable spectroscopic binary. Because of this, the target was promoted to our list of planetary candidates despite the lack of high resolution imaging needed to rule out potential blend events.

2.3. High precision radial velocities with HARPS

High-precision radial velocities (RVs) were obtained from the HARPS spectrograph mounted on the 3.6m telescope at La Silla between October and December of 2015 in order to measure the reflex motion of the star due to the hypothetical planet producing the transit signal. The observations covered our predicted negative and positive quadratures, along with epochs in between, in order to probe possible long-term trends in the RVs indicative of a possible massive companion. 23 spectra were taken in total with the simultaneous Thorium-Argon mode; the HARPS pipeline (DRS, version 3.8) was used to reduce these spectra and to obtain the (drift-corrected) radial velocities, which are calculated via cross-correlation with a G2V mask which is appropriate for the stellar type of the host (see §3.1). The typical precision was ~ 3 m/s for each individual RV measurement. For each spectra, the bisector span, S -index, and the integrated flux of the H_{α} and He I lines were obtained to monitor the activity of the host star and study its influence on the RVs (Santos et al., 2010; Jenkins et al., 2011). The measured RVs, along with these various calculated activity indicators, are given in Table 1. Although the times are given in UTC, they were converted to TBD (which is the time scale used by Kepler) for our joint analysis, which we describe in §3.2.

2.4. Archival and New Imaging

Archival imaging was obtained from the STScI Digitized Sky Survey⁸ at the EPIC coordinates of our target. Data are from the Palomar Observatory Sky Survey (POSS). In Figure 2 we show the best images among the available archival images in terms of the measured FWHM. We show images taken at two epochs and with two filters: one obtained in 1995 using the RG610 filter (red⁹, 590 – 715 nm), taken by the POSSII-F and one using the RG9 filter (near-infrared¹⁰, 700 – 970 nm) obtained in 1996 by the POSSII-N. For reference, we show the aperture used to obtain our K2 photometry (black circle, $12''$) along with circles with $5''$ (white solid line) and $2''$ (white dashed line) radii which are centered on the centroid of our target star, which was obtained by fitting a 2D Gaussian to the intensity profile.

⁸ http://stdata.stsci.edu/cgi-bin/dss_form

⁹ Transmission curve available at <http://www.cadc-ccda.hia-ihp.nrc-cnrc.gc.ca/en/dss/TransmissionCurves>,

¹⁰ Transmission curve available at <http://www.cadc-ccda.hia-ihp.nrc-cnrc.gc.ca/en/dss/TransmissionCurves>,

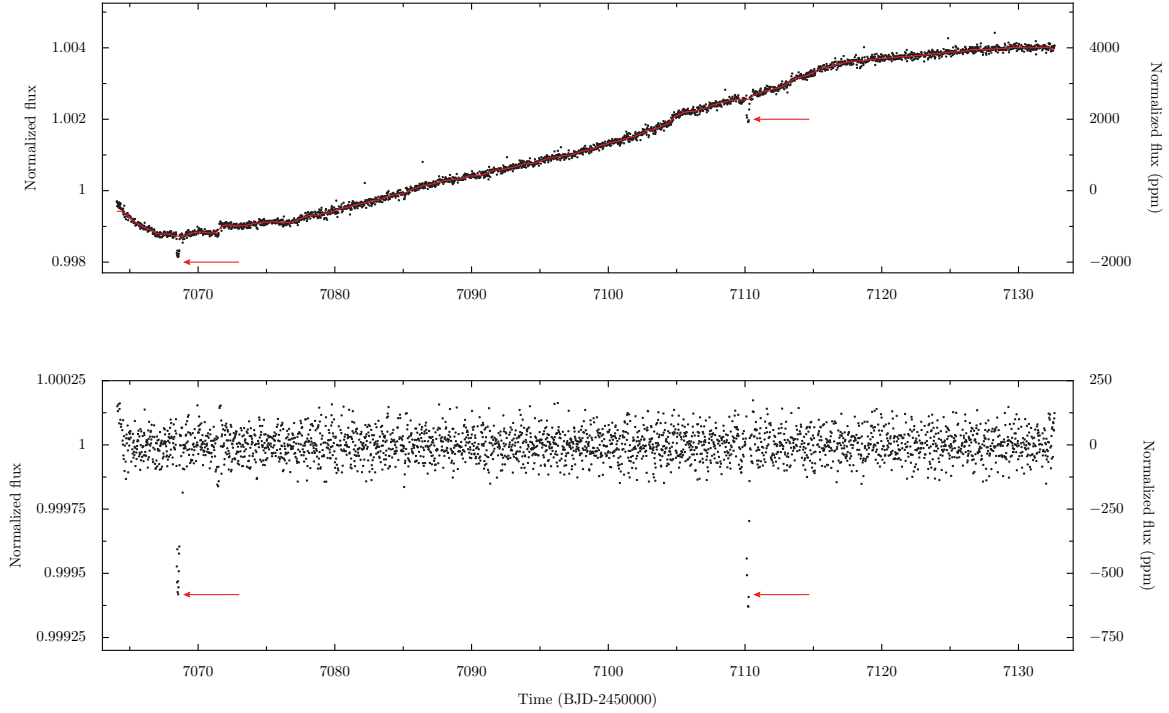


Figure 1. K2 photometry (obtained from Vanderburg & Johnson, 2014, upper panel) and long-term and outlier corrected version of the photometry (lower panel). The smooth, long-term variation observed in the original photometry was removed by a smoothed median-filter, depicted in the upper panel by a red solid line, which was used for outlier removal (see text). Two clear transit-like events can be seen on both versions of the photometry close to 2457070 and 2457110 BJD (indicated with red arrows). Note that the precision obtained for this lightcurve is ~ 55 ppm (rms) per point.

Table 1
Radial velocities obtained with the HARPS spectrograph along with various activity indicators.

BJD (UTC)	RV m sec^{-1}	σ_{RV} m sec^{-1}	BIS m sec^{-1}	σ_{BIS} m sec^{-1}	$S_{H,K}$ dex	$\sigma_{S_{H,K}}$ dex	H_{α} dex	$\sigma_{H_{\alpha}}$ dex	He I dex	$\sigma_{H_{\alpha}}$ dex
2457329.63450	-20333.9	4.4	35.0	6.2	0.1748	0.0063	0.10151	0.00013	0.50230	0.00081
2457329.67362	-20340.1	3.6	28.9	5.0	0.1535	0.0050	0.10337	0.00013	0.50279	0.00081
2457329.72375	-20337.9	3.9	34.2	5.6	0.1864	0.0053	0.10367	0.00013	0.50146	0.00081
2457330.80181	-20343.1	2.6	22.6	3.7	0.1483	0.0035	0.10167	0.00013	0.50787	0.00082
2457331.63418	-20342.5	2.4	23.2	3.4	0.1551	0.0029	0.10171	0.00013	0.51233	0.00083
2457331.68695	-20338.4	2.0	11.0	2.8	0.1573	0.0026	0.10209	0.00013	0.50301	0.00081
2457332.64705	-20335.7	2.6	20.2	3.7	0.1549	0.0038	0.10236	0.00013	0.50221	0.00081
2457332.72713	-20338.4	2.0	12.9	2.9	0.1459	0.0025	0.10178	0.00013	0.50273	0.00081
2457336.65528	-20345.3	3.2	20.8	4.5	0.1701	0.0042	0.10397	0.00013	0.49984	0.00081
2457336.73328	-20339.8	3.6	9.5	5.1	0.1547	0.0047	0.10187	0.00013	0.49884	0.00081
2457339.70924	-20343.1	4.9	14.2	6.9	0.1985	0.0068	0.09939	0.00013	0.49982	0.00081
2457339.72063	-20339.2	4.1	31.1	5.8	0.1738	0.0058	0.10496	0.00013	0.50575	0.00082
2457340.69354	-20340.0	3.7	5.9	5.3	0.1833	0.0056	0.10217	0.00013	0.51486	0.00083
2457340.70475	-20336.6	3.1	23.9	4.3	0.1687	0.0044	0.10083	0.00013	0.50038	0.00081
2457341.74523	-20336.6	3.3	18.7	4.7	0.1658	0.0043	0.10536	0.00013	0.50213	0.00081
2457341.75600	-20335.3	3.2	25.4	4.5	0.1491	0.0043	0.10274	0.00013	0.50658	0.00082
2457348.80101	-20330.3	3.1	21.6	4.4	0.1858	0.0056	0.10339	0.00013	0.50277	0.00081
2457360.62435	-20337.2	2.2	14.8	3.2	0.1581	0.0029	0.10354	0.00013	0.50080	0.00081
2457360.63915	-20336.8	2.1	11.0	3.0	0.1585	0.0027	0.10237	0.00013	0.50273	0.00081
2457361.66418	-20337.3	3.1	30.7	4.4	0.1719	0.0042	0.10607	0.00013	0.50020	0.00081
2457361.67814	-20337.0	2.9	32.8	4.1	0.1533	0.0038	0.10231	0.00013	0.49660	0.00080
2457362.66191	-20331.0	2.2	15.4	3.1	0.1517	0.0031	0.10313	0.00013	0.49866	0.00081
2457362.67602	-20335.6	2.2	13.5	3.1	0.1575	0.0032	0.10479	0.00013	0.50121	0.00081

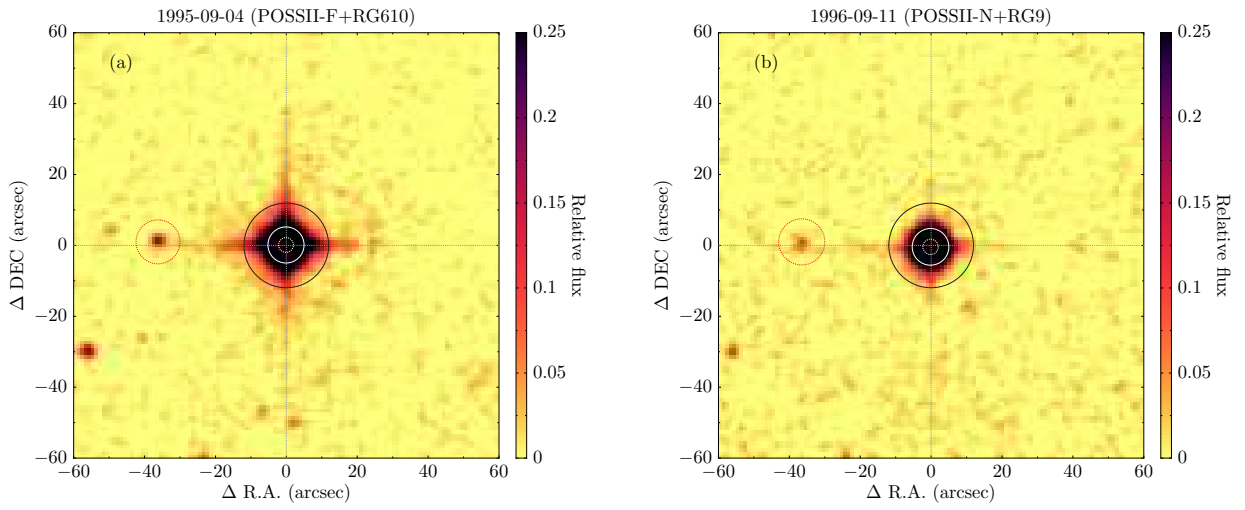


Figure 2. Archival imaging for our target at the coordinates given in the EPIC catalog obtained with different versions of POSS: (a) POSSII-F survey, taken with a red filter and (b) POSSII-N survey, taken with an infrared filter. The black circle indicates the aperture used for our K2 data. The white solid circle has a radius of $5''$ and the dashed circle a radius of $2''$ for illustration purposes; these are centered on the measured centroid of the target star. The red circle to the left of the target star marks an object which is ~ 8.2 magnitudes fainter than the target in R (see text).

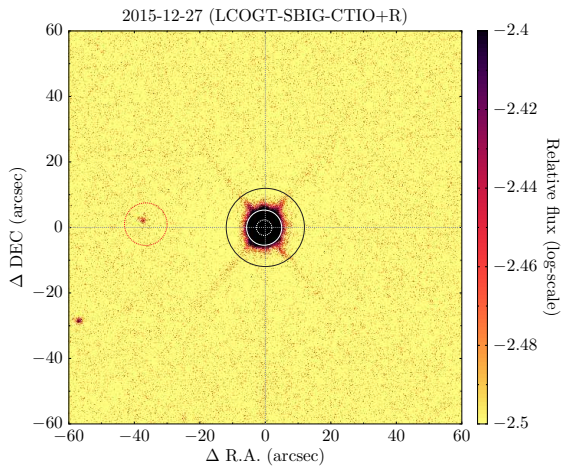


Figure 3. Modern imaging of our target obtained from LCOGT from CTIO using the SBIG camera with the R filter on 2015/12/27. Note that, although the circles have the same meanings as the ones in Figure 2, the scale here is different.

New imaging was obtained using the Las Cumbres Observatory Global Telescope Network (LCOGT). Four images were taken using the SBIG camera with the Bessel R filter on UT 2015/12/27 from the Cerro Tololo Inter-American Observatory (CTIO). Our target star reached close-to saturation counts (~ 47000 counts) in order to have enough photons to observe the close-by stars present in the POSS images. Figure 3 shows the resulting image obtained by median-combining our four images, along with the same circles as those drawn on Figure 2.

Given that the largest potential source of false-positive detections in our case comes from blended eclipsing binary systems mimicking a planetary transit event, we note that, given that the depth of the observed transit is $\sim 0.05\%$, if a blended eclipsing binary system was responsible of the observed depth, then assuming a total eclipse of the primary (which is the worst case scenario; all other scenarios should be easier to detect), the eclipsed star would have to be ~ 8.23 magnitudes fainter than our target star in the *Kepler* bandpass. We can confidently rule out such a bright star down to a distance of $9''$ of the target star with the POSSII and LCOGT images. For reference, the closest star to the left of the target star (indicated with a red circle) in Figures 2 and 3 is ~ 8.2 magnitudes fainter than the target star in the R band. As can be seen on the images, a star that bright would be evident in the archival POSS images and/or on our new LCOGT images at distances larger than $9''$.

2.5. Adaptive optics & lucky imaging

Adaptive optics (AO) imaging was obtained using MagAO+Clío2 instrument mounted at the Magellan Clay telescope in Las Campanas Observatory on December 6th using the K_s filter with the full Clío2 1024×512 pixel frames of the narrow camera ($f/37.7$). The natural guide star system was used and, because our target is relatively bright, it was used as the guide star. 32 images with exposure times of 30 sec each were taken in five different positions of the camera (nodding), all of them at different rotator offset angles. Due to a motor failure of the instrument, the nodding and rotation patterns were not able to cover the full $16'' \times 8''$ field of view around the star. However, it gave us enough data to rule

out stars within a $2''$ radius. We follow methods similar to those described in Morzinski et al. (2015) to reduce our images, which we briefly describe here; a Python implementation of such methods is available at Github¹¹. First, the images were corrected by dark current but not flat fielded, because the flats show an uneven flux level as a result of optical distortions and not of intrinsic pixel sensitivities (see section A.3 in Morzinski et al., 2015, for a detailed explanation of this effect). A bad pixel mask provided by Morzinski et al. (2015) was used in order to mask bad pixels. After these corrections are applied to each image, we obtain a median image using our 32 frames in order to get an estimate of the background flux, which we then subtract from each of the individual frames. In order to further correct for differences in the sky backgrounds of each image, we apply a 2D median filter with a 200 pixel ($\approx 3''$) window which takes care of large-scale fluctuations of each image. The background-subtracted images are then merged by first rotating them to the true north (using the astrometric calibration described in Morzinski et al., 2015) and combined using the centroid of our target star (obtained by fitting a 2D Gaussian to the profile) as a common reference point between the images. Our resulting AO image, obtained by combining our 32 images, is shown in Figure 4. A 2D gaussian fit to the target star gives a FWHM of $0''.2$, which we set as our resolution limit.

The limiting contrasts in our AO observations in the K_s band were estimated as follows. First, a 2D gaussian fit to the target star was made and used to remove it from the image. Although a 2D gaussian does not perform a perfect fit at the center, the fit is good enough for the wings of the PSF, which is our aim. Then, at each radial distance $n \times \text{FWHM}$ away from the target star, where $n = 1, 2, \dots, 15$ is an integer, a fake source was injected at 15 different angles. Sources with magnitude differences from 11 to 0 were injected in 0.1 steps, and a detection was defined if 3 or more pixels were 5-sigma above the median flux level at that position. The results of our injection and recovery experiments are plotted in Figure 5.

Only one source was detected at $\sim 2''$ from the target. The shape and position of this object is inconsistent with a speckle but is very faint: we measure a magnitude difference of $\Delta K_s = 9.8$ with the target and is thus just above our contrast level at that position (see Figure 4, the source is indicated with a grey circle in the upper right). A careful assessment of the PSF shape, however, made it inconsistent with the object having the same PSF shape as our star. Comparing its PSF with known “ghosts” on the image, on the other hand, revealed that this source is not of astrophysical but of instrumental origin.

In order to search for companions at larger separations, lucky imaging was obtained with AstraLux Sur mounted on the New Technology Telescope (NTT) at La Silla Observatory (Hippler et al., 2009) on 2015/12/24 using the i' band. Figure 4 shows our final image obtained by combining the best 10% images with a drizzle algorithm. Because the PSF shape obtained for our lucky imaging is complex and we already ruled out companions inside a $2''$ radius with Magellan+Clío2, and given that our objective with lucky imaging was to rule out companions

¹¹ <https://github.com/nespinoza/ao-reduction>

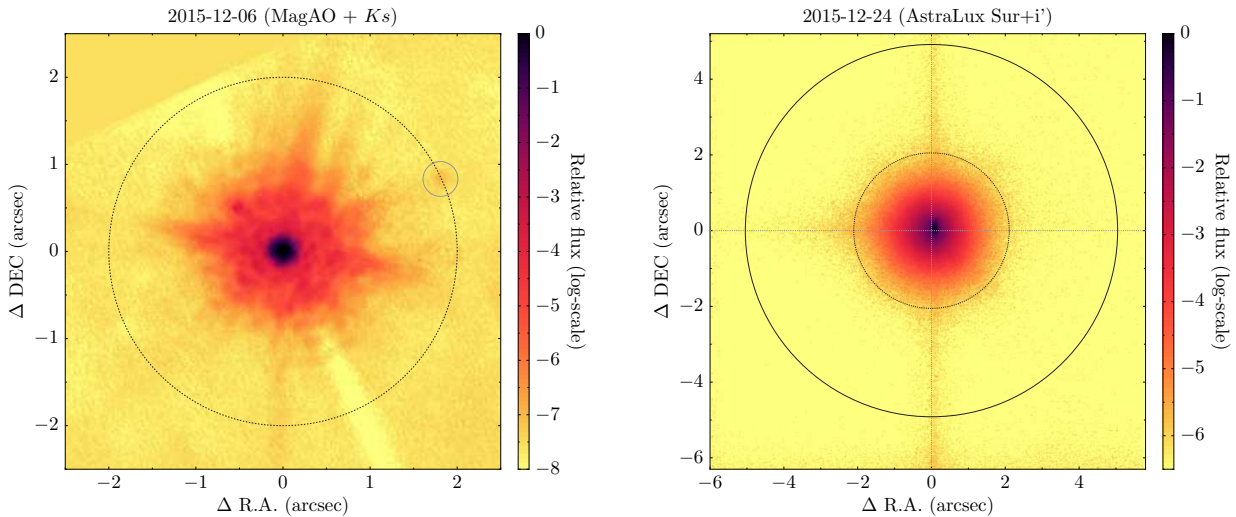


Figure 4. (Left) Adaptive optics image (log-scale) obtained with MagAO+Clío2 on 2015-12-06. The black dashed circle has a $2''$ radius for illustration and comparison with Figure 2; the grey circle mark a faint source found on our image, which was above our contrast limit but we identified as being of instrumental origin (see text). (Right) AstraLux Sur i' -band observations of our candidate on 2015-12-24. The inner black dashed circle indicates $2''$, while the outer black solid circle indicates $5''$ for comparison with Figure 2.

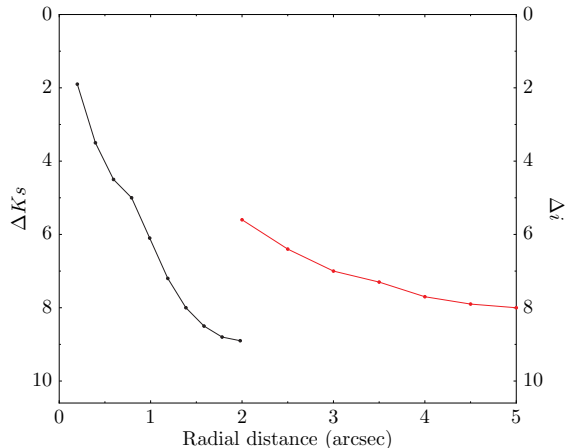


Figure 5. $5\text{-}\sigma$ contrast curves obtained from our MagAO+Clío2 K_s band (black line) and AstraLux Sur i' -band (red line) observations of our candidate.

at larger angular distances, we did not perform PSF subtraction algorithms in order to obtain the $5\text{-}\sigma$ contrasts at those distances. Instead, we used simple aperture photometry in order to estimate the $5\text{-}\sigma$ contrasts outside the $2''$ radius by performing a procedure similar to that described in Wöllert et al. (2015). In summary, we estimated the noise level in a 5×5 box at each radial distance at 15 different angles for distances larger than $2''$ from the estimated centroid of the image (where the contribution of the target star’s PSF to the background level is low), and calculated the magnitude contrast by obtaining the flux of the target star using a 5-pixel radius around it and a 5-pixel radius about the desired distance from the star, where $5\text{-}\sigma$ counts are summed to each pixel at that distance before performing the aperture photometry. Then, the magnitude contrast at a given distance is obtained as the average value obtained at the different angles. The resulting $5\text{-}\sigma$ contrasts are presented in Figure 5. We study the constraints that our archival, new, AO and lucky imaging put on the false-positive probabilities and transit dilutions on the next section.

3. ANALYSIS

3.1. Stellar properties

In order to obtain the properties of the host star, we made use of both photometric and spectroscopic observables of our target. For the former, we retrieved B, V, g, r and i photometric magnitudes from the AAVSO Photometric All-Sky Survey (APASS, Henden & Munari, 2014) and J, H and K photometric magnitudes from 2MASS for our analysis. For the spectroscopic observables, we used the Zonal Atmospheric Stellar Parameter Estimator (ZASPE, Brahm et al., 2016) algorithm using our HARPS spectra as input. ZASPE estimates the atmospheric stellar parameters and $v \sin i$ from our high resolution echelle spectra via a least squares method against a grid of synthetic spectra in the most sensitive zones of the spectra to changes in the atmospheric parameters. ZASPE obtains reliable errors in the parameters, as well as the correlations between them by assuming that the principal source of error is the systematic mismatch between the data and the optimal synthetic spectra, which arises from the imperfect modelling of the stellar atmosphere or from poorly determined parameters of the atomic transitions. We used a synthetic grid provided by Brahm et al. (2016) and the spectral region considered for the analysis was from 5000 \AA to 6000 \AA , which includes a large number of atomic transitions and the pressure sensitive Mg Ib lines. The resulting atmospheric parameters obtained through this procedure were $T_{\text{eff}} = 5766 \pm 99 \text{ K}$, $\log(g) = 4.5 \pm 0.08$, $[\text{Fe}/\text{H}] = -0.15 \pm 0.05$ and $v \sin(i) = 3.3 \pm 0.31 \text{ km/s}$. With these spectroscopic parameters at hand and the photometric properties, we made use of the Dartmouth Stellar Evolution Database (Dotter et al., 2008) to obtain the radius, mass, age and distance to the host star using isochrone fitting with the *isochrones* package (Morton et al., 2015). We take into account the uncertainties in the photometric and spectroscopic observables to estimate the stellar properties, using the *emcee* (Foreman-Mackey et al., 2013) implementation of the affine invariant Markov Chain Monte Carlo (MCMC) ensemble sampler proposed in Goodman & Weare (2010) in order to explore the posterior parameter space. We

Table 2
Stellar parameters of BD+20594.

Parameter	Value	Source
Identifying Information		
EPIC ID	210848071	EPIC
2MASS ID	03343623+2035574	2MASS
R.A. (J2000, h:m:s)	03 ^h 34 ^m 36.23 ^s	EPIC
DEC (J2000, d:m:s)	20°35′57.23″	EPIC
R.A. p.m. (mas/yr)	36.7 ± 0.7	UCAC4
DEC p.m. (mas/yr)	−51.8 ± 1.3	UCAC4
Spectroscopic properties		
T_{eff} (K)	5766 ± 99	ZASPE
Spectral Type	G	ZASPE
[Fe/H] (dex)	−0.15 ± 0.05	ZASPE
log g_* (cgs)	4.5 ± 0.08	ZASPE
$v \sin(i)$ (km/s)	3.3 ± 0.31	ZASPE
Photometric properties		
K_p (mag)	11.04	EPIC
B (mag)	11.728 ± 0.044	APASS
V (mag)	11.038 ± 0.047	APASS
g' (mag)	11.352 ± 0.039	APASS
r' (mag)	11.872 ± 0.050	APASS
i' (mag)	10.918 ± 0.540	APASS
J (mag)	9.770 ± 0.022	2MASS
H (mag)	9.432 ± 0.022	2MASS
K_s (mag)	9.368 ± 0.018	2MASS
Derived properties		
M_* (M_{\odot})	0.961 ^{+0.032} _{−0.029}	isochrones+ZASPE
R_* (R_{\odot})	0.928 ^{+0.055} _{−0.040}	isochrones+ZASPE
ρ_* (g/cm ³)	1.70 ^{+0.20} _{−0.26}	isochrones+ZASPE
L_* (L_{\odot})	0.88 ^{+0.15} _{−0.12}	isochrones+ZASPE
Distance (pc)	152.1 ^{+9.7} _{−7.4}	isochrones+ZASPE
Age (Gyr)	3.34 ^{+1.95} _{−1.49}	isochrones+ZASPE

Note. Logarithms given in base 10.

obtain a radius of $R_* = 0.928_{-0.040}^{+0.055} R_{\odot}$, mass $M_* = 0.961_{-0.029}^{+0.032} M_{\odot}$, age of $3.3_{-1.5}^{+1.9}$ Gyr and a distance to the host star of $152.1_{-7.4}^{+9.7}$ pc. The distance to the star was also estimated using the spectroscopic twin method described in Jofré et al. (2015), which is independent of any stellar models. The values obtained were 158.3 ± 5.4 pc when using 2MASS J band photometry and 160.0 ± 5.7 pc if H band photometry was used instead, where the stars HIP 1954, HIP 36512, HIP 49728 and HIP 58950 were used as reference for the parallax. Those values are in very good agreement with the value obtained from isochrone fitting. The stellar parameters of the host star are summarized in Table 2.

3.2. Joint analysis

We performed a joint analysis of the photometry and the radial velocities using the **EXO**planet traNsits and r**Ad**Ial veLocity fitt**ER**, **exonailer**, which is made publicly available at Github¹². For the transit modeling, **exonailer** makes use of the **batman** code (Kreidberg, 2015), which allows the user to use different limb-darkening laws in an easy and efficient way. If chosen to be free parameters, the sampling of the limb-darkening coefficients is performed in an informative way using the triangular sampling technique described in Kipping

(2013). For the quadratic and square-root laws, we use the transformations described in Kipping (2013) in order to sample the physically plausible values of the limb-darkening coefficients. For the logarithmic law we use the transformations described in Espinoza & Jordán (2016), which presents the sampling of the limb darkening parameters for the more usual form of the logarithmic law to allow for easier comparison with theoretical tables (if the geometry of the system is properly taken into account, see Espinoza & Jordán, 2015). The code also allows the user to fit the lightcurve assuming either a pure white-noise model or an underlying flicker ($1/f$) noise plus white-noise model using the wavelet-based technique described in Carter & Winn (2009). For the RV modelling, **exonailer** assumes Gaussian uncertainties and adds a jitter term in quadrature to them. The joint analysis is then performed using the **emcee** MCMC ensemble sampler (Foreman-Mackey et al., 2013).

For the joint modelling of the dataset presented here, we tried both eccentric and circular fits. For the radial velocities, uninformative priors were set on the semi-amplitude, K , and the RV zero point, μ . The former was centered on zero, while the latter was centered on the observed mean of the RV dataset. Note that our priors allow us to explore negative radial velocity amplitudes, which is intentional as we want to explore the possibility of the RVs being consistent with a flat line

¹² <http://www.github.com/nespinoza/exonailer>

(i.e., $K = 0$). Initially a jitter term was added but was fully consistent with zero, so we fixed it to zero in our analysis. As for the non-circular solutions, flat priors were set on e and on ω instead of fitting for the Laplace parameters $e \cos(\omega)$ and $e \sin(\omega)$ because these imply implicit priors on the parameters that we want to avoid (Anglada-Escudé et al., 2013). For the lightcurve modelling, we used the selective resampling technique described in Kipping (2010) in order to account for the 30 min cadence of the K2 photometry, which has as a consequence the smearing of the transit shape. In order to minimize the biases in the retrieved transit parameters we fit for the limb darkening coefficients in our analysis (see Espinoza & Jordán, 2015). In order to decide which limb-darkening law to use, we apply the method described in Espinoza & Jordán (2016) which, through simulations and given the lightcurves properties, aids in selecting the best limb-darkening law in terms of both precision and bias using a mean-squared error (MSE) approach. In this case, the law that provides the minimum MSE is the quadratic law, and we use this law in order to parametrize the limb-darkening effect. In addition, the K2 photometry is not good enough to constrain the ingress and egress times because only two transits were observed in long-cadence mode, which provides poor phase coverage; this implies that the errors on a/R_* are rather large. Because of this, we took advantage of the stellar parameters obtained with our HARPS spectra, and derived a value for this parameter from them (see Sozzetti et al., 2007) of $a/R_* = 54.83^{+2.19}_{-3.16}$. This value was used as a prior in our joint analysis in the form of a Gaussian prior. We used the largest of the errorbars as the standard deviation of the distribution, which is centered on the quoted median value of the parameter¹³. We tried both fitting a flicker-noise model and a white-noise model, but the flicker noise model parameters were consistent with no $1/f$ noise component, so the fit was finally obtained assuming white noise. 500 *walkers* were used to evolve the MCMC, and each one explored the parameter space in 2000 links, 1500 of which were used as burn-in samples. This gave a total of 500 links sampled from the posterior per *walker*, giving a total of 250000 samples from the posterior distribution. These samples were tested to converge both visually and using the Geweke (1992) convergence test.

Figures 6 and 7 show close-ups to the phased photometry and radial velocities, respectively, along with the best-fit models for both circular (red, solid line) and non-circular (red, dashed line) fits obtained from our joint analysis of the dataset. The lightcurve fits for both models are very similar, but in the RVs the differences are evident. In particular, the eccentric fit gives rise to a slightly smaller semi-amplitude than (yet, consistent with) the one obtained with the circular fit. For the eccentric fit, we obtain $e = 0.096^{+0.089}_{-0.066}$, $\omega = 53^{+17}_{-23}$ degs and a semi-amplitude of $K = 2.9^{+1.1}_{-1.0}$ m sec⁻¹. For the circular orbit, we find a semi-amplitude of $K = 3.1^{+1.1}_{-1.1}$ m sec⁻¹. Since the differences on the lightcurves are very small,

¹³ Performing a joint analysis with a large uniform prior on a/R_* spanning from $a/R_* \in (25, 70)$ gives a posterior estimate of $a/R_* = 55.92^{+5.64}_{-13.11}$ for this parameter, which is in excellent agreement with this spectroscopically derived value.

we analyze the likelihood function of the radial-velocity data in order to compare the models and decide which is preferred by the data. We obtain that both models are indistinguishable, with both the AIC ($\Delta\text{AIC} = 2$) and BIC ($\Delta\text{BIC} = 2$) values being ~ 2 . We thus choose the simpler model of those two, which is the circular model, and report the final parameters using this as our final model.

The resulting parameters of our fit are tabulated in Table 3. It is interesting to note that the radial velocity semi-amplitude is inconsistent with zero by almost 3σ . Moreover, we are confident that those variations do not arise from activity as all the correlation coefficients we calculate between our RVs and the different activity indexes given in Table 1 give correlation coefficients which are consistent with 0 at $\approx 1\sigma$, and all variations of the activity indices at the period and time of transit-center found for our target are consistent with flat lines. Interestingly, the radial-velocity semi-amplitude is large for a planetary radius of only $R_p = 2.23^{+0.14}_{-0.11} R_\oplus$; the $K = 3.1^{+1.1}_{-1.1}$ m/s semi-amplitude implies a mass of $M_p = 16.3^{+6.0}_{-6.1} M_\oplus$, which at face value could be consistent with a rocky composition, a rare property for a Neptune-sized exoplanet such as BD+20594b. We caution, however, that this interpretation has to be taken with care, as we have poor phase coverage on the “up” quadrature. We put these values in the context of discovered exoplanets of similar size in §4.

3.3. Planet scenario validation

In order to validate the planet scenario which we have implied in the past sub-section, we make use of the formalism described in Morton (2012) as implemented on the publicly available *vespa*¹⁴ package. In short, *vespa* considers all the false-positive scenarios that might give rise to the observed periodic dips in the light curve and, using photometric and spectroscopic information of the target star, calculates the false-positive probability (FPP) which is the complement of the probability of there being a planet given the observed signal. Because our archival and modern imaging presented on §2.4 rule out any companion at distances larger than $9''$ radius, we consider this radius in our search for possible false-positive scenarios using *vespa*, which considers the area around the target star in which one might suspect false-positives could arise. The algorithm calculates the desired probability as

$$\text{FPP} = \frac{1}{1 + f_p P},$$

where f_p is the occurrence rate of the observed planet (at the specific observed radius) and $P = L_{\text{TP}}/L_{\text{FP}}$, where TP indicates the transiting-planet scenario and FP the false-positive scenario, and each term is defined as $L_i = \pi_i \mathcal{L}_i$, where π_i is the prior probability and \mathcal{L}_i is the likelihood of the i -th scenario. For our target, considering all the information gathered and the fact that no secondary eclipse larger than ≈ 165 ppm (i.e., 3-sigma) is detected, we obtain a value of $P = 4288.79$. As for the occurrence rate of planets like the one observed, we

¹⁴ <https://github.com/timothymorton/VESPA>

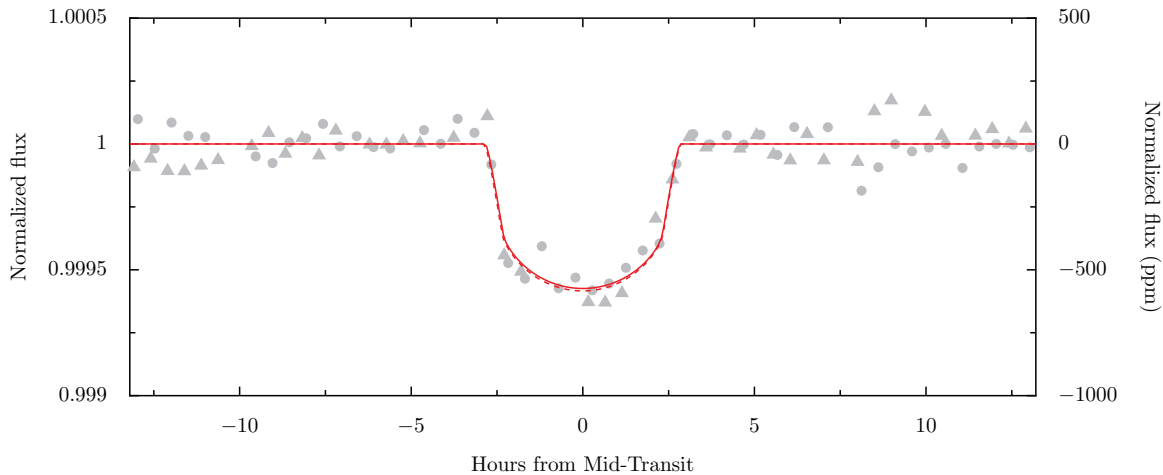


Figure 6. Phase-folded photometry (grey points; circles the first transit, triangles the second transit) and best-fit transit lightcurve for the circular (red, solid line) and eccentric (red, dashed line) fits for our planet obtained from our joint analysis. Note that the difference in the lightcurve for both fits is very small.

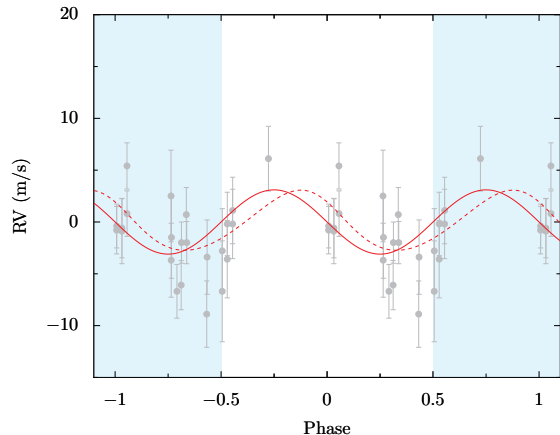


Figure 7. Phase-folded HARPS radial velocities (grey) and best-fit radial velocity models for both circular (red, solid line) and eccentric (red, dashed line) fits using our joint analysis. The light blue bands indicate regions that have been repeated for better visualisation of the RV curve.

consider the rates found by Petigura, Marcy & Howard (2013) for planets between $2 - 2.83R_{\oplus}$ with periods between 5 and 50 days orbiting solar-type stars, which is 7.8%, i.e., $f_p = 0.078$. This gives us a false-alarm probability of $FPP = 3 \times 10^{-3}$. Given that this probability is smaller than the usual 1% threshold (e.g., Montet et al., 2015), we consider our planet validated. We note that this FPP is an upper limit on the real FPP given our AO and lucky-imaging observations. Both observations rule out an important part of the parameter space for blending scenarios between $0''.2$ and $5''$ from the star, which are the main source of false-positives for our observations.

3.4. Transit dilutions

As it will be discussed in the next section, both the planet radius and mass puts BD+20594 in a very interesting part of the mass-radius diagram. Therefore, it is important to discuss the constraints that our spectroscopic and new, AO and lucky imaging observations pose on possible background stars that might dilute the transit depth and thus cause us to underestimate the transit radius.

Given that the factor by which the planetary radius is

Table 3
Orbital and planetary parameters for BD+20594.

Parameter	Prior	Posterior Value
Lightcurve parameters		
P (days)	$\mathcal{N}(41.68, 0.1)$	$41.6855^{+0.0030}_{-0.0031}$
$T_0 - 2450000$ (BJD _{TDB})	$\mathcal{N}(7151.90, 0.1)$	$7151.9021^{+0.0042}_{-0.0047}$
a/R_{\star}	$\mathcal{N}(54.83, 3.16)$	$55.8^{+3.3}_{-3.3}$
R_p/R_{\star}	$\mathcal{U}(0, 0.1)$	$0.02204^{+0.00058}_{-0.00057}$
i (deg)	$\mathcal{U}(80, 90)$	$89.55^{+0.17}_{-0.14}$
q_1	$\mathcal{U}(0, 1)$	$0.38^{+0.29}_{-0.16}$
q_2	$\mathcal{U}(0, 1)$	$0.52^{+0.32}_{-0.30}$
σ_w (ppm)	$\mathcal{J}(50, 80)$	$55.00^{+0.73}_{-0.72}$
RV parameters		
K (m s^{-1})	$\mathcal{N}(0, 100)$	$3.1^{+1.1}_{-1.1}$
μ (km s^{-1})	$\mathcal{N}(-20.337, 0.1)$	$-20.33638^{+0.00073}_{-0.00073}$
e	—	0 (fixed)
Derived Parameters		
M_p (M_{\oplus})	—	$16.3^{+6.0}_{-6.1}$
R_p (R_{\oplus})	—	$2.23^{+0.14}_{-0.11}$
ρ_p (g/cm^3)	—	$7.89^{+3.4}_{-3.1}$
$\log g_p$ (cgs)	—	$3.50^{+0.14}_{-0.21}$
a (AU)	—	$0.241^{+0.019}_{-0.017}$
V_{esc} (km/s)	—	$30.2^{+5.3}_{-6.2}$
T_{eq} (K)	—	—
Bond albedo of 0.0	—	546^{+19}_{-18}
Bond albedo of 0.75	—	386^{+13}_{-12}

Note. Logarithms given in base 10. $\mathcal{N}(\mu, \sigma)$ stands for a normal prior with mean μ and standard-deviation σ , $\mathcal{U}(a, b)$ stands for a uniform prior with limits a and b and $\mathcal{J}(a, b)$ stands for a Jeffrey's prior with the same limits.

changed by a collection of stars inside the aperture used to obtain the photometry of the target star is given by $\sqrt{1/F_{\%}}$, where $F_{\%}$ is the fraction of the total flux in the aperture added by the star being transited, we estimate that only stars with magnitude differences $\lesssim 2$ are able to change the transit radius by magnitudes similar to the quoted uncertainties in Table 3. We note that such

magnitude differences in the Kepler bandpass are ruled out from $0''.2$ to the aperture radius used to obtain the photometry for our target star: our AO and lucky imaging observations rule out companions of such magnitudes from $0''.2$ to $5''$ (see Figure 5). On the other hand, stars with magnitude differences of that order should be evident on our retrieved archival and new images presented in §2.4, at least at distances of $5''$ from our target star, and up to and beyond the $12''$ aperture used to obtain the K2 photometry. Given that the remaining unexplored area on the sky is very small (only $0''.2$ around our target star), and that a star of such magnitude should produce an evident peak on the cross-correlation function on our high resolution spectra which is not seen, we consider that our derived transit radius is confidently unaffected by dilutions of background field stars.

4. DISCUSSION

As mentioned in the previous section, the large mass ($M_p = 16.3_{-6.1}^{+6.0} M_\oplus$) for the calculated radius ($R_p = 2.23_{-0.11}^{+0.14} R_\oplus$) found for BD+20594b is very interesting. Figure 8 compares BD+20594b with other discovered exoplanets with radii less than $4R_\oplus$ (\sim Neptune) and masses smaller than $32M_\oplus$ (limits of theoretical models) as retrieved from exoplanets.eu¹⁵ except for the Kepler-10 planets, for which we use the masses obtained by Weiss et al. (2016), along with 2-layer models obtained from Zeng, Sasselov & Jacobsen (2016). As can be seen, BD+20594b spans a regime in radius at which most exoplanets have low densities and are composed of large amounts of volatiles (Rogers, 2015). In particular, taking the mass-radius estimates for BD+20594b at face value, the best-fit composition assuming a 2-layer model for the planet is 100% MgSiO_3 , i.e., a pure rock composition, positioning the planet in the boundary of “possibly rocky” and “non-rocky” planets. More realistic three-layer alternatives, however, can explain the observed radius and mass of the planet if a rock/Fe core has an added volatile envelope, composed either by water or H/He (see, e.g., the modelling for Kepler-10c in Weiss et al., 2016). If, for example, we assume an Earth-like interior composition for the planet (i.e., 74% MgSiO_3 and 26% Fe) and again take the mass and radius estimates at face value, three-layer models obtained from Zeng, Sasselov & Jacobsen (2016) give a possible $0.2R_\oplus$ water envelope for the planet (corresponding to 8% in mass). This thus gives a maximum radius for a possible H/He envelope, which would anyways produce a small layer of much less than a percent in mass; at least significantly smaller than the one modelled for Kepler-10c.

Given that the errors on the mass of BD+20594b are large enough to be consistent with several compositions, a careful assessment must be made in order to explore its possible rocky nature. To this end, we follow the approach introduced by Rogers (2015) and compute p_{rocky} , the posterior probability that a planet is sufficiently dense to be rocky, which is defined as the fraction of the joint mass-radius posterior distribution that falls between a planet composition consistent with being rocky. A probably rocky planet, then, would have $p_{\text{rocky}} \sim 1$, while a planet with a density that is too low

to be rocky would result in $p_{\text{rocky}} \sim 0$. The definition of “rocky planet” used in Rogers (2015), which we adopt in this work, is given by those planets spanning compositions between 100% rock and 100% Fe. Although this definition is based on simple 2-layer models for the planetary composition, and in theory for a given point in the mass-radius diagram planets could have denser compositions with a gaseous envelope on top, we use this metric anyways in order to compare our newly discovered exoplanet in terms of the population of already discovered small planets. This is an important point to make, as p_{rocky} is actually an upper limit on the probability that a planet is indeed rocky. To compute this value and compare it to the population of exoplanets with secure masses and radii discovered so far, we use the models from Zeng, Sasselov & Jacobsen (2016). To sample from the posterior distributions given the posterior estimates published in the literature for the different exoplanets, we use the methods described in Appendix A of Espinoza & Jordán (2015) and assume these radii and masses are drawn from skew-normal distributions in order to use the asymmetric error bars published for those parameters, while we use the posterior samples of our MCMC fits described in §3.2 to sample from the posterior joint distribution of mass and radius of BD+20594b. Our results are depicted in Figure 9, where we also indicate the threshold radius found by Rogers (2015) at which there is a significant transition between rocky and non-rocky exoplanets, with smaller exoplanets having in general rocky compositions and larger exoplanets having less dense compositions.

As evident in Figure 9, BD+20594b is in an interesting position in this diagram. The closest exoplanet to BD+20594b in this diagram is Kepler-20b, which has a radius of $1.91_{-0.21}^{+0.12} R_\oplus$, which is only $2 - \sigma$ away from the “rocky” boundary. BD+20594b, on the other hand, is more than $5 - \sigma$ away from it. With a value of $p_{\text{rocky}} \sim 0.43$, BD+20594b is the first Neptune-sized exoplanet to date with a large (compared to the typical Neptune-sized planet) posterior probability of being dense enough to be rocky.

The large mass obtained for BD+20594b implies that if the planet ever had the chance to acquire an atmosphere, it should retain it. However, if the planet is indeed actually primarily composed of rock, given its small radius, a significant H/He envelope is unlikely in the usual settings of planet formation. Calculations using core accretion theory by Ikoma & Hori (2012), predict that if the mass of rock in the protoplanet is on the order of $\sim 10M_\oplus$, even for disk dissipation time-scales on the order of $\sim 10\text{kyr}$ an accretion of a $\sim 1M_\oplus$ H/He envelope should happen. Even in the case of a large opacity of the protoplanetary disk, a mass of rock similar to the one possible for BD+20594b should imply at least this level of H/He accretion. Given the bulk composition and distance of BD+20594b to its parent star, mass loss due to X-ray and Extreme UV radiation from its parent star is unlikely. If this indeed is the primary composition of this planet, it might be possible that it formed at late stages in the protoplanetary disk, under conditions similar to those on transition disks (Lee & Chiang, 2016) or that some external effect removed the accreted envelope

¹⁵ Data retrieved on 23/12/2015

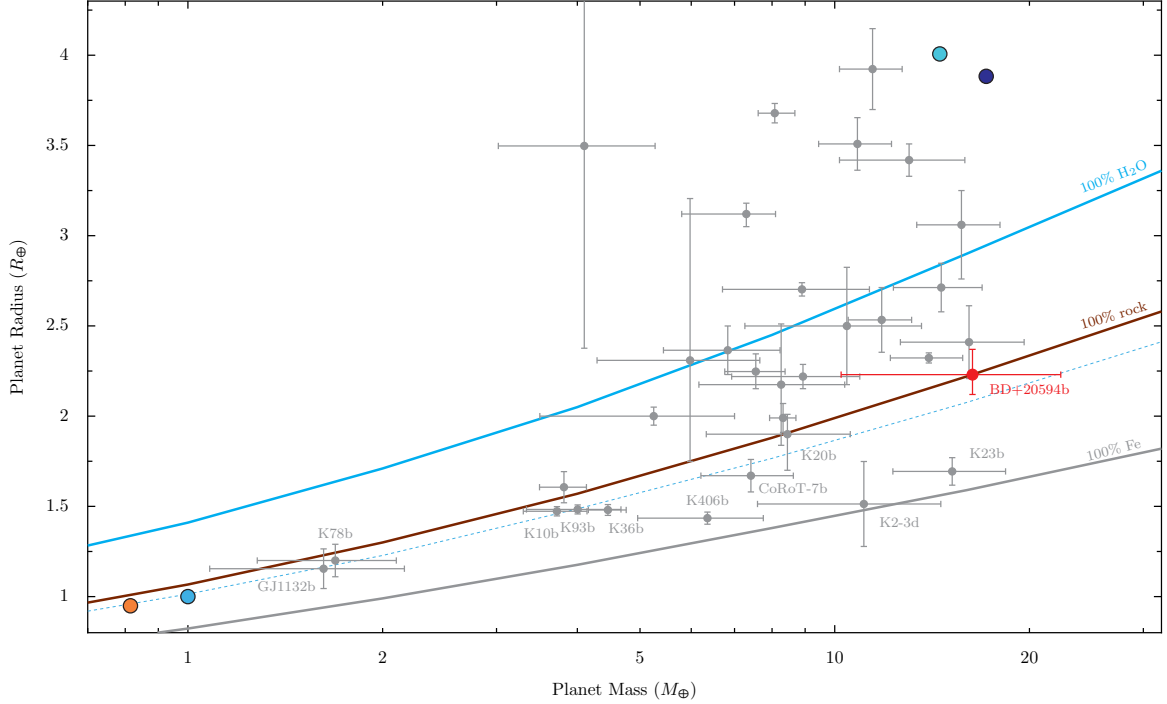


Figure 8. Mass-radius relationship for planets with secure masses and radii (at the $3 - \sigma$ level, grey points) having masses less than $32M_{\oplus}$ and radii less than $4R_{\oplus}$. BD+20594b is plotted in red, while Solar System planets are plotted as coloured circles (on the lower left Earth with blue, Venus with orange, and in the upper right Neptune in cyan and Uranus in dark blue). Theoretical 2-layer mass-radius models from Zeng, Sasselov & Jacobsen (2016) are plotted with different colors; a 100% water composition is depicted in blue, a 100% rock (MgSiO_3) composition in brown and a 100% Fe composition in grey. The light blue dashed line indicates the best-fit composition of small rocky exoplanets obtained by Zeng, Sasselov & Jacobsen (2016) for reference (74% MgSiO_3 , 26% Fe); the best-fit composition of BD+20594b is that of 100% MgSiO_3 .

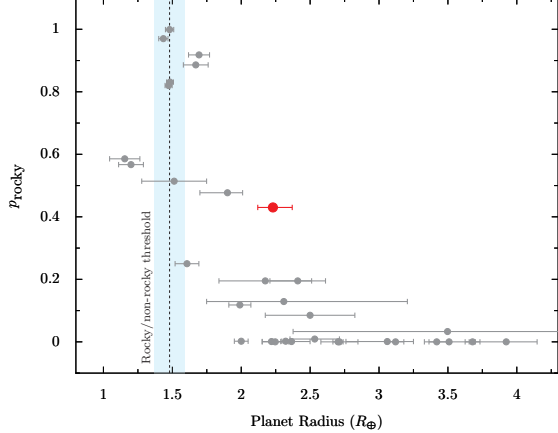


Figure 9. The posterior probability that a planet is sufficiently dense to be rocky, p_{rocky} , as a function of radius for all exoplanets with secure masses and radii (grey points), along with the estimated values for BD+20594b (red point). The black dashed line shows the transition between rocky (to the left) and non-rocky (to the right of the diagram) planets, along with the 95% confidence band on this threshold (blue band).

from the planet. Recent studies on giant impacts, which predict efficient devolatilization mechanisms for Super-Earths, might prove useful in explaining the lack of an extended atmosphere for BD+20594b if the planet ever accreted a significant H/He atmosphere in the first place (Liu et al., 2015).

In terms of mass and radius, BD+20594b is similar to both Kepler-131b (Marcy et al., 2014) and Kepler-10c (Weiss et al., 2016). Although both of them are probably non-rocky due to their low p_{rocky} (~ 0.1 and

~ 0.002 respectively), which is the main difference with BD+20594b, they are also “warm” Neptune-sized planets just as BD+20594b, with periods of $16d$ and $45.29d$, respectively. The similarity in mass, radius and period between Kepler-10c and BD+20594b, in fact, makes both of these planets excellent laboratories for comparison in order to put planet formation theories to test.

Finally, it is interesting to mention that the sub-solar metallicity of the host star adds more weight to the growing evidence that low-mass planets tend to be found orbiting stars with a lower metallicity content (Mayor et al., 2009; Adibekyan et al., 2012) or at least they appear to show a lack of preference towards metal-rich stars (Jenkins et al., 2013; Buchhave & Latham, 2015).

5. CONCLUSIONS

Using K2 photometry from Campaign 4 and a follow-up effort including radial-velocities from the HARPS spectrograph, we have presented BD+20594b, a planet with a radius $R_p = 2.23^{+0.14}_{-0.11} R_{\oplus}$ and mass of $M_p = 16.3^{+6.0}_{-6.1} M_{\oplus}$ orbiting a solar-type star. BD+20594b lies in an interesting position in the mass-radius diagram, in the boundary between “possibly rocky” and “non-rocky” planets. Given the brightness of the host star ($V = 11.04$), BD+20594b is amenable for future follow-up studies, which will enable a detailed study of its mass and hence composition, that might be able to confirm whether BD+20594b is in the “possibly rocky” or “non-rocky” regime on the mass-radius diagram.

6. ACKNOWLEDGMENTS

We thank the referee for insightful comments that greatly improved this work. N.E., J.S.J. and A.J. would like to thank E. Pallé for his willingness to share time on northern hemisphere facilities for follow-up efforts. N.E. and R.B. are supported by CONICYT-PCHA/Doctorado Nacional. A.J. acknowledges support from FONDECYT project 1130857 and from BASAL CATA PFB-06. N.E., R.B. A.J. and J.C. acknowledge support from the Ministry for the Economy, Development, and Tourism Programa Iniciativa Científica Milenio through grant IC 120009, awarded to the Millennium Institute of Astrophysics (MAS). J.S.J. acknowledges support from BASAL CATA PFB-06. This paper includes data collected by the Kepler mission. Funding for the Kepler mission is provided by the NASA Science Mission directorate. It also made use of the SIMBAD database (operated at CDS, Strasbourg, France), NASA's Astrophysics Data System Bibliographic Services, and data products from the Two Micron All Sky Survey (2MASS) and the APASS database and the Digitized Sky Survey. Based on observations collected at the European Organisation for Astronomical Research in the Southern Hemisphere under ESO programmes 096.C-0499(A), 096.C-0417(A) and 096.D-0402(A).

REFERENCES

- Adibekyan, V. Zh., Sousa, S. G., Santos, N. C., et al., 2012, *A&A*, 545, 32.
- Almenara, J.-N., Astudillo-Defru, N., Bonfils, X., 2015, *A&A*, 581, L7.
- Anglada-Escudé, G., Rojas-Ayala, B., Boss, A.P., et al., 2013, *A&A*, 551, A48.
- Armstrong, D., Santerne, A., Veras, D., et al., 2015, 582, A33.
- Becker, J., Vanderburg, A., Adams, F. C., Rappaport, S. A., Schwengeler, H. M., et al., 2015, *ApJL*, 812, 2.
- Berta-Thompson, Z., Irwin, J., Charbonneau, D., et al., 2015, *Nature*, 527, 204.
- Brahm et al., 2016, in prep.
- Borucki, W. J., Koch, D. G., Basri, G., et al., 2011, *ApJ*, 728, 117.
- Buchhave & Latham, 2015, *ApJ*, 808, 107.
- Carter, J. A., Agol, E., Chaplin, W., et al., 2012, *Science*, 337, 556.
- Carter, J & Winn, J, 2009, *ApJ*, 704, 51.
- Crossfield, I., Petigura, E., Schlieder, J., et al., 2015, *ApJ*, 804, 10.
- Dotter, A., Chaboyer, B., Jevremović, D., et al., 2008, *ApJS*, 178, 89.
- Dressing, C. D., Charbonneau, D., Dumusque, X., et al., 2015, *ApJ*, 800, 135.
- Dumusque, X., Bonomo, A., Haywood, R., et al., 2015, *ApJ*, 789, 154.
- Espinoza, N. & Jordán, A., 2015, *MNRAS*, 450, 1879.
- Espinoza, N. & Jordán, A., 2016, *MNRAS*, in press.
- Ford, E., Fabrycky, D., Steffen, J., et al., 2012, *ApJ.*, 750, 113.
- Foreman-Mackey, D., Hogg, D., Lang, D. & Goodman, J., 2013, *PASP*, 125, 306.
- Fressin, F., Torres, G., Rowe, J., et al., 2012, *Nature*, 482, 195.
- Geweke, J., 1992, *Bayesian Statistics*, 169.
- Goodman, J. & Weare, J., 2010, *Comm. App. Math. Comp. Sci.*, 5, 65.
- Grunblatt, S. K., Howard, A. W., Haywood, R. D., 2015, *ApJ*, 808, 2.
- Hadden, S. & Lithwick, Y., 2014, *ApJ*, 787, 80.
- Henden, A. & Munari, U., 2014, *Contributions of the Astronomical Observatory Skalnaté Pleso*, 518.
- Hippler, S., Bergfors, C., Brandner, W., et al., 2009, *The Messenger*, 137, 14.
- Howard, A., Sanchis-Ojeda, R., Marcy, G., 2013, *Nature*, 503, 381.
- Ikoma, M., & Hori, Y., 2012, *ApJ*, 753, 66.
- Jenkins, J. S., Murgas, F., Rojo, P., et al., 2011, *A&A*, 531, A8.
- Jenkins, J. S., Jones, H. R. A., Tuomi, M., et al., 2013, *ApJ*, 766, 67.
- Jofré, P., Mädler, T., Gilmore, G., et al., 2015, *MNRAS*, 453, 1428.
- Jordán, A., Brahm, R., Bakos, G. Á., et al. 2014, *AJ*, 148, 29.
- Kipping, D. M., 2010, *MNRAS*, 408, 1758.
- Kipping, D. M., 2013, *MNRAS*, 435, 2152.
- Kovács, G., Zucker, S. & Mazeh, T., 2002, *A&A*, 391, 369.
- Kreidberg, L., 2015, *PASP*, 127, 1161.
- Lee, E. & Chiang, E., 2016, *ApJ*, 817, 2.
- Léger, A., Rouan, D., Schneider, J., et al., 2009, *A&A*, 506, 287.
- Liu, S.-F., Hori, Y., Lin, D. N. C., Asphaug, E., 2015, *ApJ*, 812, 164.
- Marcy, G., Isaacson, W., Howard, A., et al., 2014, *ApJS*, 210, 20.
- Mayor, M., Udry, S., Lovis, C., et al., 2009, *A&A*, 493, 639.
- Montet, B., Morton, T., Foreman-Mackey, D., et al., 2015, *ApJ*, 809, 25.
- Morton, T., 2012, *ApJ*, 761, 6.
- Morton, T., et al., 2015, 10.5281/zenodo.16304.
- Morzinski, K., Males, J. R., Skemer, A. J., et al., 2015, *ApJ*, 815, 108.
- Pepe, F., Collier-Cameron, A., Latham, D., *Nature*, 503, 377.
- Queloz, D., Bouchy, F., Moutou, C., et al., 2009, *A&A*, 506, 303.
- Petigura, E., Marcy, G. & Howard, A., 2013, *ApJ*, 770, 69.
- Petigura, E., Schlieder, J., Crossfield, I., et al., 2015, 811, 102.
- Rogers, L., 2015, *ApJ*, 801, 41.
- Sanchis-Ojeda, R., Rappaport, S., Winn, J., et al., 2013, *ApJ*, 774, 54.
- Sanchis-Ojeda, R., Rappaport, S., Pallé, E., et al., 2015, 812, 112.
- Santos, N. C., Gomes da Silva, J., Lovis, C., Melo, C., 2010, *A&A*, 511, A54.
- Sozzetti, A., Torres, G., Charbonneau, D., et al., 2007, *ApJ*, 664, 1190.
- Stumpe, M., Smith, J., Van Cleve, J., et al., 2012, *PASP*, 124, 985.
- Vanderburg, A. & Jonson, J., 2014, *PASP*, 126, 948.
- Vanderburg, A., Montet, B., Johnson, J. A., et al., 2015, 800, 59.
- Weiss, L. & Marcy, G, 2014, *ApJL*, 783, L6.
- Weiss, L., Rogers, L. A., Isaacson, H. T., et al., 2016, *ApJ* in press.
- Wolfgang, A. & Lopez, E., 2015, *ApJ*, 806, 183.
- Wöllert, M., Brandner, W., Bergfors, C., et al., 2015, *A&A*, 575, A23.
- Zeng, L., Sasselov, D., & Jacobsen, S., 2016, eprint arXiv:1512.08827.